



Article

Detection of *Aspergillus flavus* in Figs by Means of Hyperspectral Images and Deep Learning Algorithms

Cristian Cruz-Carrasco ¹, Josefa Díaz-Álvarez ^{1,*}, Francisco Chávez de la O ², Abel Sánchez-Venegas ¹ and Juan Villegas Cortez ³

¹ Computer Architecture Department, University of Extremadura, C. Santa Teresa de Jornet, 38, 06800 Mérida, Spain; cristiancruzcarasco999@gmail.com (C.C.-C.); abelsv@unex.es (A.S.-V.)

² Computer and Telematics Systems Department, University of Extremadura, C. Santa Teresa de Jornet, 38, 06800 Mérida, Spain; fchavez@unex.es

³ Systems Department, Universidad Autónoma Metropolitana, Mexico City 02128, Mexico; juanvc@azc.uam.mx

* Correspondence: mjdiaz@unex.es

Abstract: Plant diseases cause economic losses and health risks, such as aflatoxins linked to liver cancer. These toxins, produced by fungi like *Aspergillus flavus* in figs, are often detected late through invasive methods or visual inspection. Since Spain, particularly Extremadura, is a key fig producer, alternative detection methods are essential to preventing aflatoxins in the food chain. The aim of this research is the early detection of *Aspergillus flavus* fungus using non-invasive techniques with hyperspectral imaging and applying artificial intelligence techniques, in particular deep learning. The images were taken after inoculation of the microtoxin using 3 different concentrations, related to three different classes and healthy figs (healthy controls). The analysis of the hyperspectral images was performed at the pixel level. Firstly, a fully connected neural network was used to analyze the spectral signature associated with each pixel; secondly, the wavelet transform was applied to each spectral signature. The resulting images were fed to a convolutional neural network. The hyperparameters of the proposed models were adjusted based on the parameter tuning process that was performed. The results are promising, with 83% accuracy, 82.75% recall, and 83.25% F1-measure for the fully connected neural network. The high F1-measure demonstrates that the model's performance is good. The model has a low incidence of false positives for samples that contain aflatoxin, while a higher number of false positives appears in healthy controls. Due to the presence of false negatives, this class also has a high recall. The convolutional neural network results, accuracy, recall, and F1 are 77.25%, indicating moderate model performance. Only class 3, with higher aflatoxin concentration, achieves high precision and low false positive incidence. Healthy controls exhibit a high presence of false negatives. In conclusion, we demonstrate the effectiveness of pixel-level analysis in identifying the presence of the fungus and the viability of the non-invasive techniques applied in improving food safety. Although further research is needed, in this study, the fully connected neural network model shows good performance with lower energy consumption.

Keywords: agriculture; deep learning; hyperspectral; imaging artificial neural network; precision agriculture



Citation: Cruz-Carrasco, C.; Díaz-Álvarez, J.; Chávez de la O, F.; Sánchez-Venegas, A.; Villegas Cortez, J. Detection of *Aspergillus flavus* in Figs by Means of Hyperspectral Images and Deep Learning Algorithms. *AgriEngineering* **2024**, *6*, 3969–3988. <https://doi.org/10.3390/agriengineering6040225>

Academic Editor: Zhengjun Qiu

Received: 16 September 2024

Revised: 17 October 2024

Accepted: 22 October 2024

Published: 28 October 2024



Copyright: © 2024 by the authors. Licensee MDPI, Basel, Switzerland. This article is an open access article distributed under the terms and conditions of the Creative Commons Attribution (CC BY) license (<https://creativecommons.org/licenses/by/4.0/>).

1. Introduction

Plant and crop diseases represent an economic cost to the agricultural and food sectors [1]. Mycotoxins are substances that are naturally produced by certain types of fungi under particular conditions of humidity and temperature. The presence of mycotoxins in food poses a serious problem for both human and animal health [2,3]. The International Agency for Research on Cancer (IARC) included a group of aflatoxins in the group 1 carcinogenic substances [4]. The common pathway of mycotoxin exposure is the ingestion of contaminated food. Identified health risks include impacts on the immune system, kidney

disease, and an increased likelihood of certain types of liver cancer [5–7]. The fungus *Aspergillus flavus*, which occurs at temperatures between 12 °C and 27 °C with 85% humidity, multiplies in foods such as maize, peanuts, rice, nuts, figs, etc, and although its presence is typical of tropical climates, it also proliferates under some irrigation conditions [8]. In this study, we focus on the proliferation of *Aspergillus flavus* fungi in fig tree fruits, especially fresh figs. The growth cycle of aflatoxin is between 3 and 5 days. Even if figs are to be dried, the introduction of aflatoxin-infected figs into the process can lead to the contamination of other fruit. Therefore, the detection of aflatoxin in the fresh product is considered crucial for both direct consumption and further processing.

The cultivation of the fig tree (*Ficus carica* L.) has its origins in the Carian region of Asia, and it has spread to other areas such as the Mediterranean region, Africa, and America. Today, Spain is the sixth largest producer in the world, accounting for 3.5%. Figs grown in Spain reached up to 21,719 ha in 2023 (17,381 dry and 4339 irrigated). The region of Extremadura with 12,771 ha (10,306 dry and 2465 irrigated) represents the largest producer in Spain [9]. In terms of production [10], Extremadura accounted for 55.5% (24,296 tonnes) of national production, which reached 43,800 tonnes in 2022 (data for 2023 are not available yet). The increase in productivity is linked to the adoption of innovative techniques such as fertilization, pruning, soil treatment, and irrigation [11,12]. Irrigation techniques are leading to a gradual increase in irrigated fig hectares and a decrease in dry fig hectares.

Arid and semi-arid areas have perfect conditions for fig trees' cultivation, but their shallow roots and prolonged droughts result in a lack of water and mineral requirements to ensure the quality of the fruit [13]. To alleviate tree stress, boost productivity, and improve fruit quality, supplemental irrigation has emerged as an effective alternative for different crops [14], including fig trees [15,16]. However, changes in humidity facilitate the spread of *Aspergillus flavus* mycotoxin, and scientists need to carry out additional research to analyze and prevent infected figs from entering the human food chain.

The Scientific and Technological Research Center of Extremadura (CICYTEX-“Finca La Orden-Valdesequera” located in Guadajira (Badajoz)) is a referent in agri-food research, including fig tree cultivation, analyzing the proliferation of the Aflatoxin before and after harvest. Just to mention a few, researchers in [17] addressed the effect of the temperature during the fig productive process, controlling the hygienic and sanitary quality of the figs. In [18], the authors evaluated the application of two treatments at the early post-harvest stages of dried figs to control mycotoxin. The authors in [19] analyzed the suitability of two yeast strains (*H. opuntiae* L479 and *H. uvarum* L793) to act as biopreservatives, to inhibit *A. flavus* growth, and to reduce aflatoxin accumulation.

Even though the detection of the aflatoxin *Aspergillus* has been extensively addressed, the most commonly used methods are intrusive, and they require the destruction of the sample. On the other hand, dried figs have been the primary focus for the application of innovative methods using AI techniques. However, fresh figs are perishable; they have a limited shelf life and are more sensitive to microbial growth [20], which alters the quality of the product and becomes a serious risk to human health. The detection of the aflatoxin *Aspergillus flavus* in fresh figs is the purpose of this study.

Hyperspectral Imaging (HSI) measures the interaction of a broad spectrum of light with a given object by acquiring hundreds of contiguous spectral bands for each pixel in an image. This ability provides detailed information about the object and reveals subtle differences in texture and chemistry. Depending on the material's composition, there is a different pattern of light absorption, reflection, or emission across a range of wavelengths. This pattern creates a unique spectral signature that represents how the material responds to each wavelength. Thus, materials and chemical changes can be identified via the analysis of the spectral signature [21].

Its performance in identifying chemical composition is faster than traditional methods, and its non-destructive characteristics meet the needs of the agriculture sector, among others [22]. Furthermore, the superficial distribution of the aflatoxin is an advantage for the analysis via HSI. Over the last decades, its application has attracted researchers' interest.

However, data provided via HSI express high dimensionality, which represents a challenge for classification algorithms. In this light, deep learning (DL) has become an innovative and non-intrusive method for analyzing and interpreting HSI data.

Deep learning is a subset of machine learning (ML) that models data using deep neural networks. A neural network consists of a set of interconnected layers of artificial neurons that learn from data by extracting high-level representations from a series of input data. Deep learning models can identify complex patterns in data and perform tasks such as image classification, speech recognition, and natural language processing by stacking multiple layers, each of which applies non-linear transformations of the data [23,24]. The use of DL to process and analyze hyperspectral images was first described in [25], where the authors proposed an approach to classification using spatially dominated information. A large number of subsequent studies reflect the interest of the scientific community [26–28].

Over the past few decades, the use of hyperspectral imaging (HSI) techniques has been on the rise as an analytical tool to improve tasks such as classification, segmentation, anomaly detection, data augmentation, and unmixing. The authors in [29] presented a spectral-spatial residual network (SSRN). The SSRN uses residual learning to mitigate the challenge of vanishing gradients when training deep networks on hyperspectral data. Just to mention a few, ref. [30] conducted a comprehensive survey of deep learning techniques for hyperspectral data processing. They highlighted the benefits of CNNs, RNNs, and transfer learning. Ref. [26] presented a multidisciplinary review outlining key applications and challenges to be addressed. The authors advocate for interdisciplinary collaboration as a way to advance deep learning techniques and optimize their potential in HSI analysis through more efficient models and better data handling strategies.

Precision agriculture represents a key instrument to increase productivity, improve crop quality, and address problems due to climate change. The development of IoT systems through the use of remotely controlled sensors, imaging with unmanned vehicles, and the ability to analyze the collected data using AI techniques has made precision agriculture a reality and a dynamic area of research. A wide range of research in this field is reported in recent literature reviews [31–34].

In this light, HSI has become a popular technique applied in a wide range of areas to identify internal and external features of objects under study. A few of these approaches include mineral mapping [35], atmospheric characterization [36], biological and medical issues [37], and food and agriculture [38,39], among others. HSI can capture fine spectral features through consecutive channels and many narrow spectral bands [40]; the larger the number of bands, the more detailed the spectral characteristics. However, not all bands include relevant information and enhance the accuracy, so removing redundant wavebands is useful to facilitate analyses [41]. HSI provides significant advantages for monitoring in the agri-food sector by enabling automated, non-destructive quality control, which helps optimize processes at every stage of production [42]. Detailed information facilitates the detection of subtle changes and improves accuracy, which is a crucial factor for the early detection of plant diseases [43].

In addition, HSI generates huge amounts of complex data that need to be analyzed. This is a resource-intensive and time-consuming task for which ML techniques, especially deep learning, are well suited [28,44,45]. During the last few decades, the use of ML in all fields of science has skyrocketed. ML makes use of a wide range of algorithms that allow computer systems to learn from data and identify patterns in order to infer outcomes. The authors in [46,47] presented comprehensive reviews focused on food sciences and safety by applying neural networks and general ML techniques, respectively.

Aflatoxins, particularly Aflatoxin B_1 , produced by *A. flavus*, are highly toxic to animals and humans. Their detection is essential to preventing contaminated food from entering the food supply [48].

Siedliska et al. [49] applied HSI with VNIR (400–1000 nm) and SWIR (1000–2500 nm) cameras on strawberries inoculated with *Botrytis cinerea* and *Collatotrichum acutatum* (900 samples each) and healthy controls (900 samples). Images were taken every 24 h,

and 19 wavelengths were selected based on the second derivative of the spectra. Using FCNN, RF, and SVM models, the FCNN performed the best.

In [50], the authors presented an extensive literature review; published studies used HSI aimed to identify fungal and mycotoxin-contaminated individual grain kernels applying different classifiers. The authors in [51] addressed the detection of aflatoxin in peanuts using a deep convolution neural network (CNN), and they achieved an accuracy of 95%. In a later work [52], they also included corn with a dimensional CNN; the accuracy was 96.2% and 92.1% for peanut and corn, respectively. Recently, ref. [53] addressed the identification of mycotoxins produced by *Aspergillus flavus* in peanuts and corn using six ML models. With an accuracy of 100% in distinguishing between healthy and infected samples, the authors pointed out that better data processing and further analysis are needed. Kim et al. [54] presented a method based on hyperspectral fluorescence, VNIR, or SWIR imaging combined with ML algorithms to detect the contamination of aflatoxin in ground maize. SWIR combined with the SVM model achieves higher accuracy and better generalization.

Contamination in figs has usually been addressed in dried figs. Just to mention a few recent ones, in [55], the authors analyzed UV light images using a deep CNN approach to detect and classify aflatoxin in dried figs. They carried out a fine-tuning process for pre-trained models and obtained a validation accuracy of 97.50%. The same authors [56] proposed a real-time method applying pre-trained models for deep feature extraction and classification. Images were acquired using light sources of different wavelengths. The best performance was achieved via SVM with an accuracy of 100% and 92.3% for contaminated and non-contaminated samples, respectively.

On the one hand, this study aims to develop an accurate method for the early detection of aflatoxins in fresh figs, which can enter the food supply directly and pose a potential risk to human health. On the other hand, detecting the infection before the drying process reduces the risk at an earlier stage. Our proposal is based on the analysis of hyperspectral images at a pixel level via non-intrusive methods such as deep learning. Two different phases can be identified in this research work. The first one is a parameter tuning phase that is responsible for finding the best parameter values for the deep learning algorithms to be applied in the next phase; the second one corresponds to the comparison of two different deep learning approaches: (i) a fully connected neural network (FCNN) that works with the hyperspectral signatures of each image pixel and (ii) a convolutional neural network (CNN) that is fed up with images obtained after applying the wavelet transform to the spectral signature of each image pixel.

2. Materials and Methods

This section describes the methodology applied to carry out this research work. Figure 1 represents the general methodology scheme, where the main steps are defined.

This study manages images of figs collected from a fig tree plantation of the calabacita variety at the “Finca La Orden-Valdesequera” located at 38°51' N, 6°40' W, altitude 184 m, in Guadajira, Spain, where CICYTEX has its headquarters. This area is characterized by a Mediterranean climate, with dry and hot summers, where the average annual temperature between 2000 and 2022 was 16.28 °C, with rainfall of 447.08 mm and reference evapotranspiration of 1296.15 mm. The soil texture was loamy loam, and the farm was provided with an irrigation system. The following section details the procedure to take hyperspectral images.

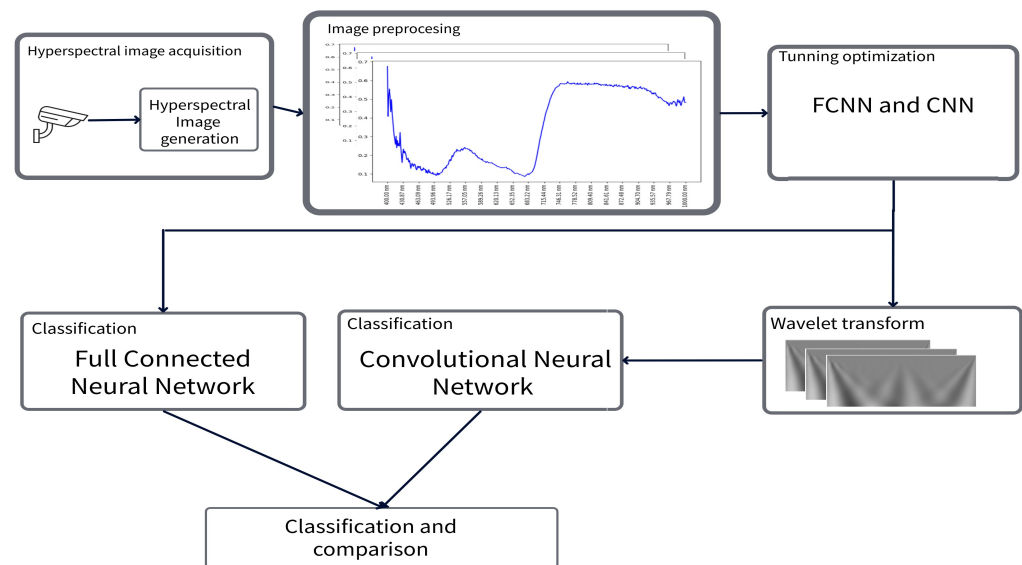


Figure 1. General scheme of the methodology followed to carry out the study.

2.1. Image Acquisition

The images were taken with a SPECIM hyperspectral camera, in particular, the model FX10 VNIR, whose main technical characteristics are as follows: spatial resolution of 1024 pixels (800 width \times 1024 height), spectral range from 400 nm to 1000 nm (VIS and part of the NIR), 448 spectral bands, and a spectral leap of 1.339.

We worked with a set of 320 figs harvested from the plantation previously mentioned. Hyperspectral images were taken for 2 weeks, each week using 160 figs harvested at different stages of maturity. Each week, the 160 figs were divided into four subsets of 40 figs. The first corresponded to the healthy controls (class 0); the following three sets of 40 figs were inoculated with a concentration of 10^3 UFC/mL (class 1), 10^5 UFC/mL (class 2), and 10^7 UFC/mL (class 3), respectively. The immersion process was carried out by immersing the area for about 3 s, according to the protocol of Cicytex, the organization responsible for this inoculation process. This ensures that the exposed area of the fruit is covered. There were no visible differences between the contaminated and uncontaminated samples, and despite varying contamination levels, no visible changes were observed in any of the samples during the experiment. Hyperspectral images were taken post-inoculation every 24 h for five days on figs that were harvested during the current week. Between each hyperspectral image acquisition session, the samples were stored in a controlled incubation room at 25 °C, where the relative humidity was between 80 and 90% to promote the growth of the fungi. The protocol followed was as follows: each day, one toxin-inoculating fig for each class was extracted for chemical analysis and tested for the presence of the toxin. Thus, the number of figs for each class, except the healthy controls, decreased daily by one unit (from 40 on the first day to 36 on the last). The inoculation process with the *A. Flavus* was performed via immersion with concentrations that had a similar surface distribution to natural aflatoxin contamination. Each class consisted of 380 hyperspectral images, giving a total of 1900 hyperspectral images.

Once acquired, the original images were pre-processed with black/white correction to normalize and correct the data. Bias can be introduced via environmental factors, lighting conditions, and sensor sensitivity, and black and white correction improves the data, removing inconsistencies and making the spectral analysis easier. This black/white correction was carried out item by item, as is shown in (1).

$$I(x, y, z) = 100 \times \frac{I_{raw}(x, y, z) - R_N(x, y, z)}{R_B(x, y, z) - R_N(x, y, z)} \quad (1)$$

where the following applies:

- I represents the hyperspectral image with normalized values of relative reflectance.
- I_{raw} is the raw hyperspectral image.
- R_N depicts the minimum reflectance or black.
- R_B represents the maximum reflectance or white.
- x, y, z are the image height, width, and depth (spectral bands).

As the inoculation procedure was carried out via immersion, the region of interest (ROI) was not the entire surface of the hyperspectral image but, rather, the lower part of each fig image.

Given that our study worked at the pixel level, it was necessary to delimit the study areas from which the pixels were to be extracted. In this light, pixel masking was carried out to identify the infected regions and extract the pixels only for these regions. This task was performed with the Labelme software (<http://labelme.csail.mit.edu/Release3.0/>, accessed on 12 February 2024), a free and open-source image annotation tool developed in Python and widely applied to label and generate masks for different types of images. Figure 2 shows an example of mask generation labeled for a set of figs.

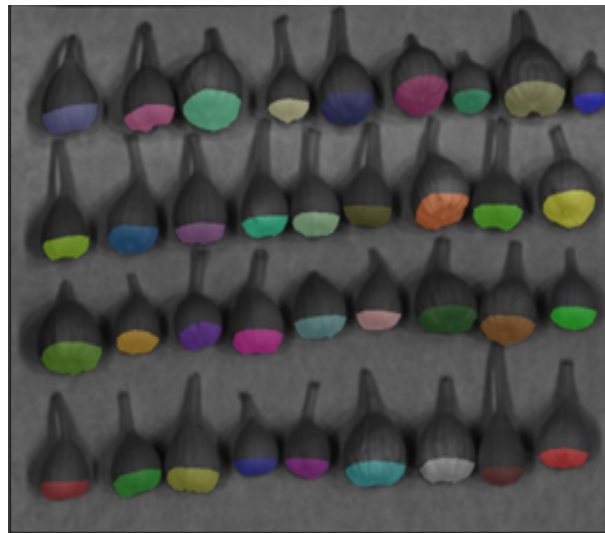


Figure 2. Pixel masking for a set of figs to extract the pixel from the region of interest using the Labelme software.

For all the images, pixels in the ROI were extracted; this process uses the coordinates of the pixels to be studied. Each pixel was extracted with its 448 spectral bands representing its features, and a new feature was included indicating the class to which it belongs. Additional information was also included to facilitate pixel identification. Figure 3 shows the shape of a fig pixel and its spectral signature.

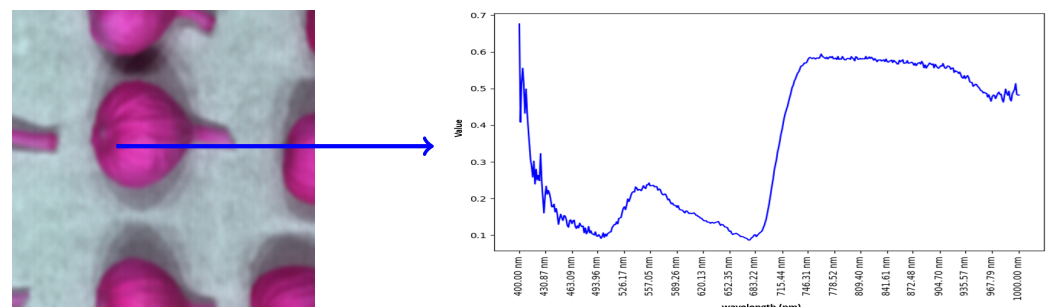


Figure 3. (Left) False RGB image of figs, obtained in hyperspectral caption process. (Right) Hyperspectral signature of a fig pixel, where the y -axis is the reflectance, and the x -axis is the wavelength.

As a result, our dataset consists of 1,330,300 hyperspectral pixels with 450 features (448 spectral bands, class labels, and pixel identification).

2.2. Data Analysis

Before using any AI technique, it is necessary to analyze the data we are working with. This section presents a brief statistical analysis before addressing the main part of this work. A spectral band was considered a predictive numerical variable, and all spectral bands obtained values between 0 and 1, as expected. Three bands stand out from the rest when taking into account the standard deviation: bands closed to ultraviolet (400–415 nm); bands between the blue and orange colors (526.17–623 nm); and bands closed to the red and infrared channels (700–1000 nm). The distribution in the first few spectral bands appears to be symmetrical, and there is a slight difference between the mean value and the median value. From 500 nm, the distribution is slightly asymmetric towards high values.

Next, the distribution of each spectral band by class was analyzed. Thus, the dataset was separated into each of the categories, and we calculated the 10th, 25th, 50th (median), 75th, and 90th percentiles, along with the maximum and minimum values. The aim was to find differences in the distribution of the bands in the different classes.

To provide more insights, Figure 4 shows details of bands in the range of 526–623 nm, comparing these distributions. In this band, there is a more marked difference in the distribution of Class 1. Class 1 is centered around higher reflectance values than the other classes. Classes 2 and 3 have a distribution centered around lower reflectance values.

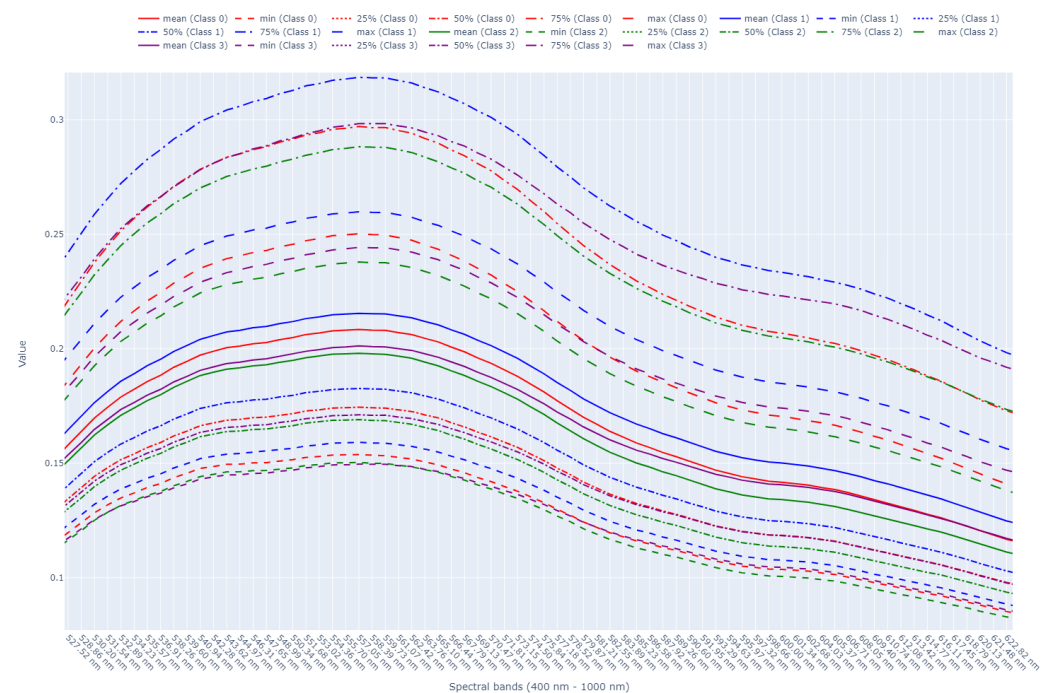


Figure 4. Statistics computed for each class per spectral band between 526.17 and 623 nm. The y-axis represents the reflectance values.

With regard to the number of instances per class, classes were balanced with 313,500, 327,500, 346,400, and 342,900 pixels belonging to classes 0, 1, 2, and 3, respectively.

The dataset was randomly divided into two different datasets, 80% for the training set (1,064,240) and 20% for the test set (266,060). In addition, 20% of the instances were randomly chosen for training validation (212,848) to avoid the over-fitting issue. Before running the different algorithms, we analyzed whether the data were balanced in both the training and test sets. Figure 5 graphically shows the balanced distribution of instances per class in training and test sets. The next section details the DL techniques and perspectives used to address this problem using a comparative point of view.

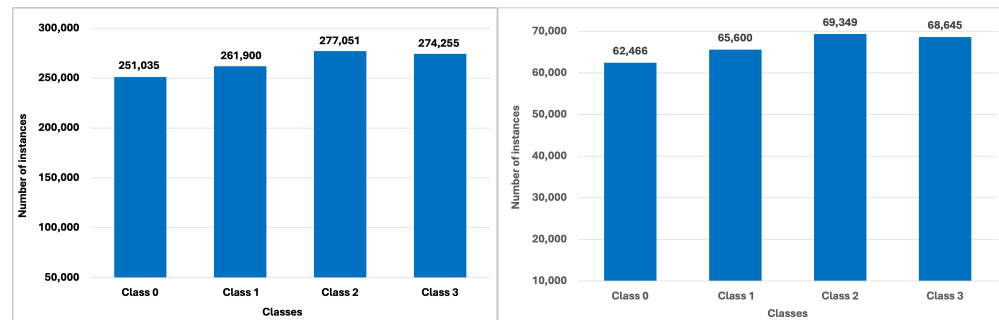


Figure 5. Number of instances per class in training and test sets, where 0 represents healthy controls, and 1, 2 and 3 are samples contaminated with different concentrations of *A. flavus*.

2.3. Deep Learning Techniques

This comparative analysis was carried out with two types of DL models, which have demonstrated their performance in a variety of research works. As DL models are really sensitive to the hyperparameter values, a hyperparameter search was performed to find the optimal ones for each model, which will be detailed in Section 2.4.1. The DL models chosen for this study were as follows.

2.3.1. FCNN

This model has an input layer of 448 neurons (pixel spectral signatures). The number of hidden layers and the number of neurons in each are determined by the hyper-parameter search. The output layer has 4 neurons corresponding to the classes. Softmax is defined as the activation function to select the class to be predicted.

2.3.2. CNN-FCNN Pipeline

This model consists of an input layer of 448, although in this case, it is a 2D image (90 px height and 448 spectral bands) after the application of the continuous wavelet transform to obtain its frequency information. Wavelet transform facilitates image compression due to its ability to localize time and frequency. The number of intermediate convolutional layers, hidden layers and their number of neurons, the activation function, and the pooling technique to be applied are determined using a hyperparameter search. The output layer has 4 neurons, and the activation function used is the softmax function.

A wavelet analysis can provide information in the frequency domain of the hyper-spectral pixel, revealing details that are missed in the time domain. Regarding the wavelet transform, the selection of the mother wavelet is crucial to obtaining a smooth, continuous wavelet amplitude and phase information. Since the complex Morlet wavelet (CWT) is a non-orthogonal, complex exponential wavelet tapered by a Gaussian function, it meets both requirements [57]. CWT, represented by Equation (2) (Pywt library—pywavelets documentation for Morlet Wavelet (“morl”)), is an effective method for image processing, and it was chosen as the mother wavelet.

$$\Psi(t) = \exp \frac{-t^2}{\cos} 5t \quad (2)$$

Figure 6 shows the architecture models for both approaches.

2.4. Sustainability Analysis

In our view, there is a need for researchers to understand the environmental impact of their AI models. AI requires a huge amount of computing power to train the models, and it can consume large amounts of energy and generate large amounts of carbon dioxide emissions. In this work, we take into account the impact of the solutions proposed during the training phase. Considering this, CodeCarbon and Green Algorithms are the only Python tools that estimate energy consumption and emissions for memory, CPU and GPU separately.

CodeCarbon tracks carbon dioxide (CO₂) emissions from ML experiments, measuring the carbon footprint in kilograms of CO_{2eq} per kilowatt-hour consumed. This tool helps estimate and minimize the environmental impact of AI models by providing accurate data on energy consumption and greenhouse gas emissions [58]. Recent studies [59] confirm that CodeCarbon provides values close to those provided via a wattmeter. In this way, both the energy consumed by memory, CPU, and GPU during the training phase of the models and the CO₂ emissions were evaluated. The results will be presented in Section 3.

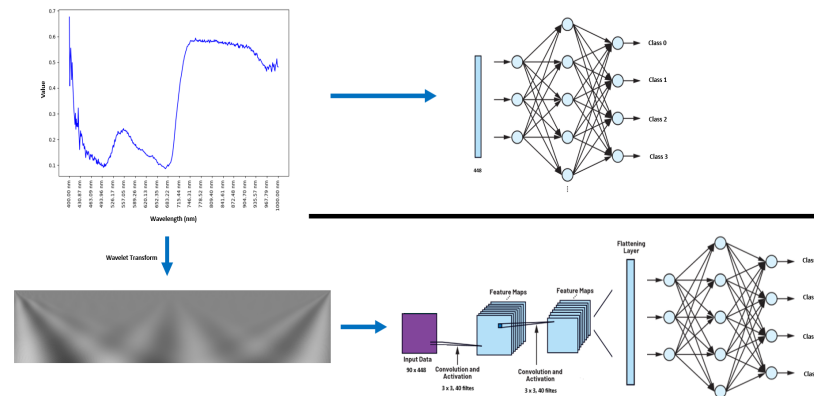


Figure 6. Architectural models for FCNN and CNN.

2.4.1. Hyperparameter Search

A hyperparameter search was carried out for both network architectures to identify those values that reached the best performance. An accuracy value of 0.7 was defined as the threshold to address the next level of hyperparameter search within a particular network setting. Table 1 shows the hyperparameters and values tested for the FCNN and CNN approaches. We used the random search method over 100 networks or a combination of hyperparameters for the FCNN approach and 40 for the CNN. Differences arise because of the excessive training time for CNN.

Table 1. Hyperparameter search for FCNN and CNN approaches.

FCNN		
Hyperparameter	Values	Description
Activation function	relu, elu, selu	Activation function in the hidden layers
Hidden layers	2–7	Number of hidden layers in the network
Neurons/hidden layer	64–4096 (in step of 32)	Number of neurons in each hidden layer
Dropout	0.0–0.3 (in step of 0.1)	Dropout for each hidden layer
CNN		
Hyperparameter	Values	Description
Activation function	relu, elu, selu	Activation function in the hidden layers
Hidden layers	1–4	Number of hidden layers in the network
Neurons/hidden layer	64–1024 (in step of 32)	Number of neurons in each hidden layer
Pooling layer	Max pooling, average pooling	Type of pooling layer

For both architecture networks, the Adam algorithm was used as the optimization function and the categorical cross-entropy as the loss function.

3. Experimental Results

This section presents and analyzes the results obtained for each model individually and comparatively. Furthermore, a comparative study of the training time, energy consumption, and carbon footprint during the training phase is shown.

The implementation of FCNN and CNN in this research was achieved with the Tensorflow library (version 2.17) and Python (version 3.9) as the programming language. Table 2 provides information concerning technical implementation regarding the computing systems used to implement the proposed methodology.

Table 2. Systems used to conduct the experiments.

DL Model	GPU	Processor	RAM	Operating System
FCNN	GeForce RTX 2080 Super	Intel Core i9-9900K	16GB	MS-Windows 11
CNN	A100-PCIE-40GB 108 cores	Intel Xeon Silver 4310	500 GB	Linux-5.15.0-97

The results were evaluated using a set of well-known metrics. The choice of evaluation metrics used in this study is not arbitrary. It responds to the need to capture different aspects of the performance of classification models.

- Accuracy provides the total percentage of correct predictions and it is useful in scenarios where the data are balanced, as our data are.
- Precision measures the proportion of instances correctly classified as positive out of those that are predicted to be positive. Precision helps minimize the number of false positives.
- Recall quantifies the number of positive class predictions with respect to all positive instances in the dataset.
- F-Measure provides a single score that balances both precision and recall in one single metric.

Additionally, the confusion matrix is provided to better understand the performance of the models and the nature of the errors (false positives or false negatives). This offers a clear overview, helping to identify areas for improving the models. As a result of analyzing the dataset to find differences in the distribution of the bands in the different classes, we can conclude that maximum values are really similar for all classes, and differences are present between 571 nm and 665 nm. Regarding minimum values, we appreciate differences in the previously mentioned range of bands (400–415 nm, 526.17–623 nm, and 700–1000 nm).

3.1. FCNN Results

As a result of the hyperparameter search, the obtained network architecture consists of eight layers, one input layer, six hidden layers, and one output layer. Regarding the hidden layers, the dropout ratio was applied between them, increasing with the network architecture. In addition, ReLU was chosen as the activating function. Figure 7 shows the FCNN settings, and Table 3 details additional information about the architecture structure.

The results achieved with this approach are shown in Table 4, which represents the confusion matrix, where columns represent the predicted class, and rows depict the real class. To clarify the results, Table 5 shows the values for all different metrics used to evaluate the model presented.

Based on the study of the effect of different culture media on the pathogenicity of *Aspergillus flavus* in fig fruits, there is no significant difference in the severity of spore infection levels (10^3 , 10^5 , and 10^7) for the cases examined. In our experiment, Class 0 was

misclassified as Class 1 in 2.47% of the total sample, as Class 2 in 4.13%, and Class 3 in 2.24%. These findings align with the confusion observed for Class 2, which shows the highest misclassification rate with Class 0. Our results indicate that hyperspectral samples are sufficiently effective for significant discrimination, achieving an F1-measure of at least 0.77 in the worst-case scenario for classifying a healthy fig and at least 0.83 for classifying an infected fig.

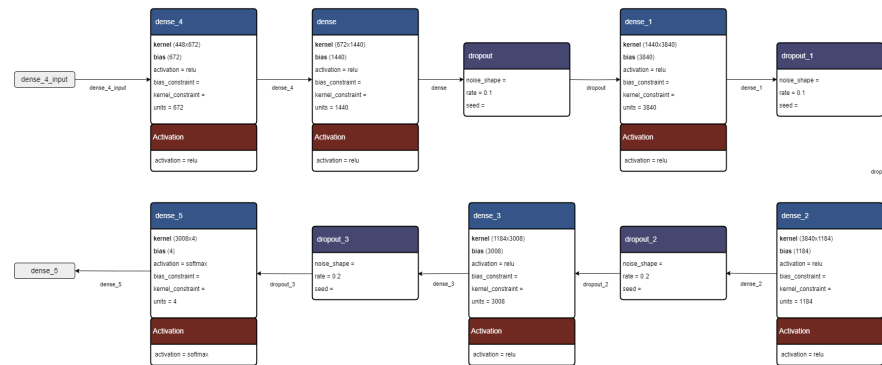


Figure 7. Setting for FCNN architecture model.

Table 3. FCNN architectural details.

Layer	Output Format	Training Settings
Layer 1 (dense)	672	301,728
Layer 2 (dense)	1440	969,120
Dropout layer	-	-
Layer 4 (dense)	3840	5,533,440
Dropout layer	-	-
Layer 6 (dense)	1184	4,547,744
Dropout layer	-	-
Layer 8 (dense)	3008	3,564,480
Dropout layer	-	-
Layer 10 (dense)	4	12,036
Total	-	14,928,548
Total	-	103,335,292

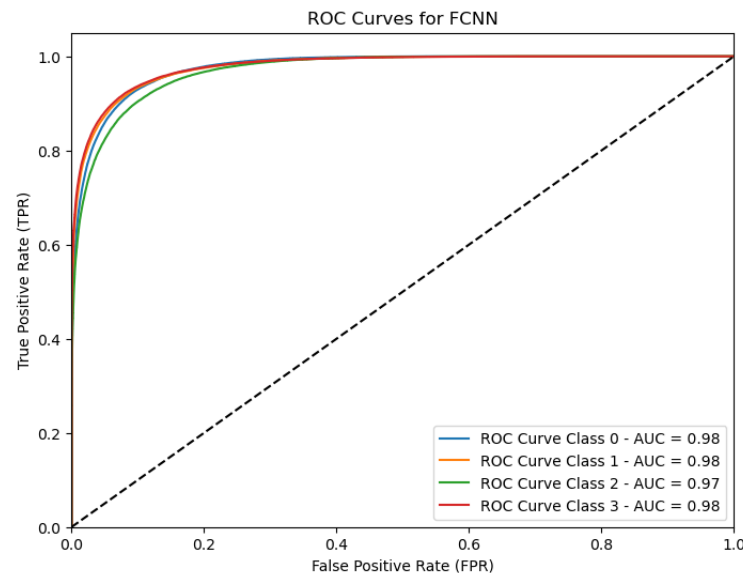
Table 4. Confusion matrix. Colored cells represent the instances correctly classified for each class (true positives) FCNN model.

		Predicted Class			
		Class 0	Class 1	Class 2	Class 3
Real Class	Class 0	56,933	1545	2585	1403
	Class 1	9271	52,593	2280	1456
	Class 2	11,031	1866	54,294	2158
	Class 3	8807	1312	2251	56,275

Table 5. Classification metrics for the FCNN model.

	Class 0	Class 1	Class 2	Class 3
Precision	0.66	0.92	0.88	0.92
Recall	0.91	0.8	0.78	0.82
F1-measure	0.77	0.86	0.83	0.87

The analysis of the results shows a good performance of the FCNN model. On average, 83% of instances are correctly classified. The next step is the individual analysis of each metric. Considering that classes 1, 2, and 3 correspond to different levels of aflatoxin inoculated, the precision metric is high, and there is a low incidence of false positives. Class 0 represents healthy controls, and the precision value is lower; consequently, the number of false positives is higher than in the other classes. Due to the low presence of false negatives in the corresponding predictions, class 0 has a higher recall value than the other classes. The F1-measure is the harmonic mean between precision and recall. Classes 1, 2, and 3, which represent the inoculated instances, obtain similarly good results, and only class 0 obtains a low value due to its low precision value. We can conclude that our model based on the spectral signature of individual pixels can identify cases inoculated with aflatoxin with high values for each metric, but it performs worse for healthy controls. To complete this analysis, we measure the goodness of the classification results generating the ROC curve for each class and computing the AUC value for each ROC curve. Figure 8 plots how well the classification model behaves for each different class. Even though further research needs to be done, the FCNN approach obtained high AUC values (≥ 0.97), which demonstrates the ability of the FCNN model to discriminate between healthy and contaminated figs for all classes.

**Figure 8.** ROC curve for the predictive model with FCNN representing the different classes.

In addition, we analyzed the environmental cost of this solution during the training phase. Table 6 presents the training time in hours, the CO₂ emissions in carbon dioxide-equivalent kilograms (CO_{2eq} Kg) and the energy consumption (KWh) for RAM, CPU, and GPU. The emission rate, which is measured in kgCO_{2eq} per hour, provides a more detailed view of the impact on the environment per unit of time. Finally, energy consumption in kilowatt-hours (kWh) measures the amount of energy consumed during the training process. These metrics are important for the assessment of the environmental and energy costs associated with the development and training of artificial intelligence models.

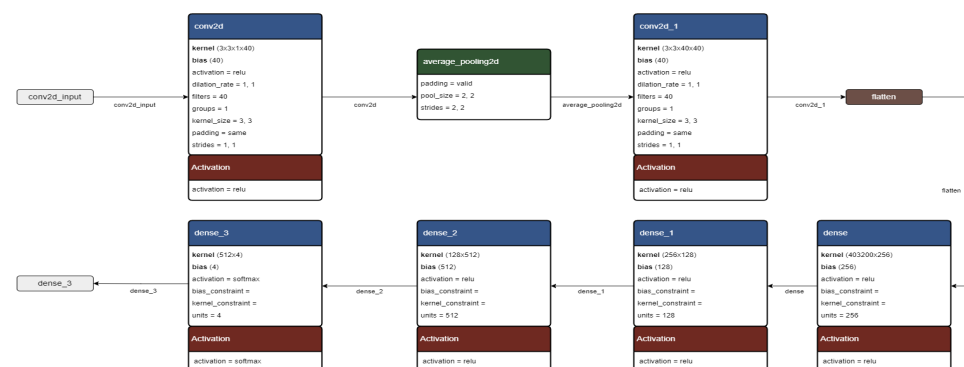
Table 6. Study of sustainability. FCNN model training time, energy consumption per component, and CO₂ emissions.

Metric	Value
Duration (h)	0.70
Emissions (CO _{2eq} Kg)	0.038
Emissions rate (CO _{2eq} Kg/h)	0.054
Energy consumption (KWh)	0.20

Although this experiment does not release a large amount of CO₂ into the atmosphere, the measurements are an important part of improving the models and reducing their environmental impact.

3.2. CNN Model

The purpose of this experiment was the processing of images after wavelet transform. It was started with the network architecture shown in Figure 9. This was the one that yielded the best result in the hyperparameter search. This architecture consists of an input layer with a number of neurons equal to the size of the image (90 px high; 448 px wide), a combination of convolutional and sequential layers (detailed in Table 7), and an output layer using *Softmax* as the activation function.

**Figure 9.** Setting for CNN architecture model.**Table 7.** CNN architectural details.

Layer	Output Format	Training Settings
Layer 1 (convolutional)	90 × 448 × 40	400
Pooling layer	45 × 224 × 40	-
Layer 2 (convolutional)	45 × 224 × 40	14,440
Flatten layer	403,200	-
Layer 3 (dense)	256	103,219,456
Layer 4 (dense)	128	32,896
Layer 5 (dense)	512	66,048
Layer 6 (dense)	4	2052
Layer 7 (dense)	256	103,219,456
Total	-	103,335,292

This experiment was conducted on a Nvidia A100-PCIE-40GB GPU because of the computational requirements. The results obtained in the test phase are detailed in the confusion matrix in Table 8, where the instances correctly predicted (main diagonal) and incorrectly predicted for each class are shown. Based on these results, precision, recall, and

F1-measure metrics are computed in Table 9 to analyze the performance of the model when predicting each class individually.

In this experiment using CNN, Class 0 was misclassified as Class 1 in 7.16% of the total sample, as Class 2 in 6.78%, and as Class 3 in 4.79%. Like the FCNN for Class 2, the largest misclassification rate occurred with Class 0. Our results indicate that hyperspectral samples are sufficiently effective for significant discrimination, achieving an F1-measure of at least 0.75 in the worst-case scenario for classifying a healthy fig and at least 0.75 for classifying an infected fig.

Table 8. Confusion matrix. Colored cells represent the instances correctly classified (true positives) for each class in the CNN model.

		Predicted Class			
		Class 0	Class 1	Class 2	Class 3
Real class	Class 0	50,759	4477	4237	2993
	Class 1	5497	51,757	4920	3426
	Class 2	7091	6501	50,437	5320
	Class 3	5220	5115	6198	52,112

Table 9. Classification metrics for the CNN model.

	Class 0	Class 1	Class 2	Class 3
Precision	0.74	0.76	0.77	0.82
Recall	0.81	0.79	0.73	0.76
F1-measure	0.77	0.78	0.75	0.79

On average, 77% of the instances were classified correctly, and this is a relatively good performance. Next, we analyze each metric individually.

The best result for the precision metric was obtained for class 3; 82% of the instances were correctly identified. Class 3 corresponds to the highest inoculated concentration. Classes 0, 1, and 2 reached 74%, 76%, and 77%, respectively. These results showed that higher concentrations of the aflatoxin are better identified with a lower number of false positives. Regarding the recall metric, all classes obtained a value of $\geq 74\%$, indicating that the model is able to identify relevant instances (true positives and false negatives). The highest value (81%) was obtained for class 0 (healthy controls). The harmonic mean between precision and recall, represented by the F1-measure, are similar; all values are in the range of [0.75–0.79]. This metric gives us information about the model's reliability; although we need to explore this issue further, the results are promising.

As was done before for the FCNN model, the ROC curve was generated for each class, and the AUC values were calculated. Figure 10 shows the results obtained, where the AUC values reveal a high discriminative power of 0.95, 0.95, 0.93, and 0.95 for classes 0, 1, 2, and 3, respectively.

As for the FCNN model, we evaluated the environmental impact of this proposal during the training phase. Table 10 presents information previously described, the training time in hours, the CO₂ emissions in carbon dioxide equivalent kilograms (CO_{2eq}Kg), and the energy consumption (KWh) for RAM, CPU, and GPU, as well as the emission rate, which is measured in kgCO_{2eq} per hour.

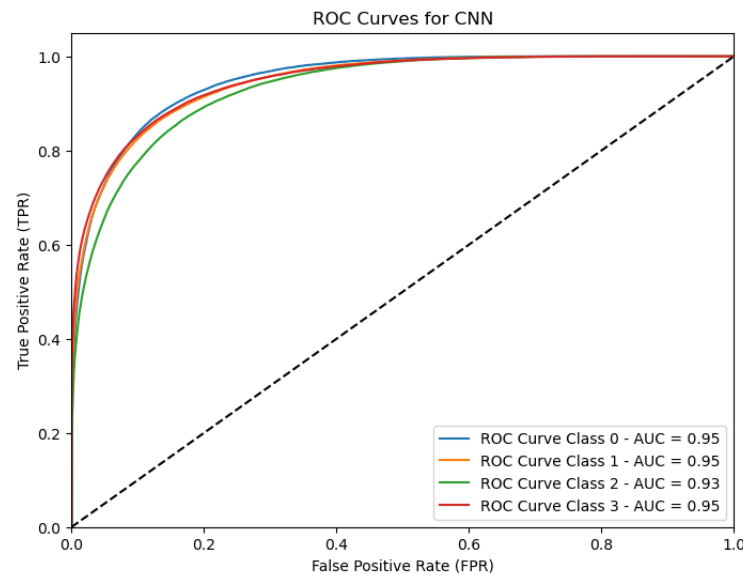


Figure 10. ROC curve for each class and AUC values for the CNN model.

Table 10. Study of sustainability. CNN model training time, energy consumption per component, and CO₂ emissions.

Metric	Value
Duration (h)	55.37
Emissions (CO _{2eq} Kg)	3.44
Emissions rate (CO _{2eq} Kg/h)	0.0623
Energy consumption (KWh)	17.75

This experiment released a significant amount of CO₂ into the atmosphere and consumed a lot of energy. In addition, the emissions and energy consumption were much higher than those of the FCNN, which achieved better performance. We must pay attention to this information for further planned research in order to reduce environmental impacts.

4. Discussion

From the results obtained, it is clear that both the FCNN and CNN models entail specific strengths and weaknesses when classifying aflatoxin-contaminated samples. However, the superior performance of the FCNN model in distinguishing samples with varying concentrations of aflatoxins is particularly noteworthy and warrants further examination. The model's ability to handle the complexity of hyperspectral image data at the pixel level demonstrates its potential for the early detection of fungal pathogens in agricultural products. Nonetheless, it is important to explore why the CNN model struggles to differentiate between contamination classes, which may be linked to its network architecture and how the wavelet-transformed hyperspectral images are processed.

The FCNN's success in identifying a greater percentage of samples compared to the CNN is partly due to its direct focus on individual pixel spectral signatures, which enhances its precision in detecting subtle differences between healthy and infected samples. However, this approach could be limited in situations where the variability between spectral signatures is minimal or where external factors such as weather conditions or the state of the crop at harvest affect the uniformity of the samples.

The FCNN shows good overall performance, especially in classes 1, 2, and 3, but class 0 needs more focus to improve its accuracy without compromising its high detection capacity. It is important to investigate whether class 0 involves patterns that are more difficult to learn. The CNN model shows solid performance, with relatively balanced metrics in

classes 0, 1, and 2, though there is room for improvement in both metrics. Improving the detection capability in classes 2 and 3 should be a priority to optimize the model's overall performance. Improvements can be approached from the following perspectives:

- Given the large difference between precision and recall in class 0 in the FCNN model, as well as the necessity of improving the identification in class 2 and reducing false negatives in class 3 for the CNN model, adjusting the model's decision thresholds can improve precision and recall.
- Different regularization techniques or hyperparameter tuning can also be explored to improve the models' ability to generalize well across all classes.
- It is important to analyze the specific characteristics of the classes to understand why the model has a lower recall for classes 2 and 3 with the CNN model and lower precision for class 0 with the FCNN model. It is possible that the features defining these classes are not sufficiently captured by the model's convolutional layers.
- Regarding the high number of false positives in healthy controls, one potential solution could involve integrating dimensionality reduction techniques to remove redundant or noisy information from hyperspectral data, which might improve the models' discrimination capabilities without compromising accuracy.

A key finding from the comparative analysis of the models is the difference in their ability to handle false positives and negatives. While both models correctly identify 68.60% of the samples, the FCNN outperforms the CNN in 14.12% of cases where the latter fails. Conversely, the CNN shows a unique ability to correctly classify 8.48% of the samples that the FCNN does not; see Table 11. This variability suggests that combining both approaches could further enhance overall performance, perhaps through a hybrid system that leverages the strengths of each architecture.

Table 11. Comparative agreement analysis between FCNN and CNN.

Result	Percentage (%)
Both models predict correctly	68.69
FCNN predict correctly/CNN fails	14.12
CNN predict correctly/FCNN fails	8.48
Both models predict incorrectly)	8.80

In addition to technical improvements, attention must be paid to optimizing these models from an environmental sustainability perspective. As previously highlighted, the CNN model's training phase consumes significantly more energy and generates higher CO₂ emissions than the FCNN. This underscores the need to balance technical performance with environmental sustainability, especially in precision agriculture, where the large-scale adoption of these technologies could have considerable implications for energy resource usage.

5. Practical Applications

To describe the practical applications of this study, it is worth mentioning that the growth cycle of aflatoxin is between 3 and 5 days. Even if figs are to be dried, introducing fruit contaminated with aflatoxins into the process can cause the contamination of other fruits. Therefore, detecting aflatoxin when in fresh products is considered crucial not only for direct consumption but also for further processing.

This research work is the first step in a series of research works specifically conducted to analyze and design AI tools that facilitate the early detection of aflatoxins in fresh figs. The incorporation of such tools into agricultural monitoring systems should become a reality and can be easily adapted to the Extremadura region. Currently, Extremadura exports 71,000 tonnes of figs worldwide, and the ability to detect infected figs in the production chain would enable the delivery of a higher-quality and healthier product.

At present, these anomalies are identified at advanced stages of the production chain, resulting in the disposal of significant quantities of produce due to minimal contamination. Detecting contaminated figs at earlier stages of the production process would significantly improve product quality (<https://higosdealmoharin.com/tag/exportacion/>, accessed on 2 October 2024).

6. Conclusions

In conclusion, this study demonstrates the feasibility of the early detection of *Aspergillus flavus* toxin in fresh figs using hyperspectral imaging combined with deep learning techniques, without the use of invasive techniques.

The FCNN model achieved an accuracy of 83%, while the CNN model performed slightly worse, with 77% accuracy. These results demonstrate the effectiveness of pixel-level analysis in identifying the presence of the fungus, both across different days and different contamination concentrations. This evidence supports the viability of the non-invasive techniques applied to improve food safety.

This study presents some limitations related to the amount of samples analyzed. However, new samples from the last harvest are being taken and will be included in subsequent research works. Additionally, a relevant number of samples have been frozen to ensure that enough samples are available to make up a huge dataset with which to train subsequent models. The main drawback is that the current models cannot be used in a production environment due to the limited availability of specific hardware and the need for more in-depth training.

Moreover, the necessity of assessing the environmental impact of AI models is underscored. During the training process, the CNN network exhibited considerably higher energy consumption and CO₂ emissions than the FCNN network. This highlights the imperative of striking a balance between technical performance and environmental sustainability in future studies. The work suggests further research into optimizing models to enhance their accuracy and reduce their ecological impact.

Finally, a fair comparison is essential in this context. However, most studies focus on dried figs, whereas fresh and dried figs differ significantly in their chemical composition. Moreover, these characteristics are influenced by factors such as climate conditions and soil composition, which vary by region. To ensure a more accurate comparison, further research using samples from the same plantation is necessary.

Author Contributions: Conceptualization, J.D.-Á. and F.C.d.l.O.; data curation, C.C.-C. and A.S.-V.; formal analysis, C.C.-C., J.D.-Á., F.C.d.l.O. and J.V.C.; funding acquisition, J.D.-Á. and F.C.d.l.O.; investigation, C.C.-C., J.D.-Á., F.C.d.l.O. and A.S.-V.; methodology, J.D.-Á. and F.C.d.l.O.; project administration, J.D.-Á.; resources, J.D.-Á. and F.C.d.l.O.; software, C.C.-C.; supervision, J.D.-Á. and F.C.d.l.O.; validation, J.D.-Á., F.C.d.l.O. and J.V.C.; writing—original draft, C.C.-C., J.D.-Á., F.C.d.l.O., A.S.-V. and J.V.C.; writing—review and editing, C.C.-C., J.D.-Á., F.C.d.l.O., A.S.-V. and J.V.C. All authors have read and agreed to the published version of the manuscript.

Funding: J.D.-Á., F.C.d.l.O. and J.V.C. are supported by the Spanish Ministry of Science and Innovation under projects PID2023-147409NB-C22 and PID2020-115570GB-C21, funded by MCIN/AEI/10.13039/501100011033 and Junta de Extremadura, project GR15068. F.C.d.l.O. is also supported by the development and innovation project PID2020-117392RR-C41, funded by MCIN/AEI/10.13039/501100011033 and by “ERDF A way of making Europe”, and the AGROS2022 project.

Data Availability Statement: Data and code will be available after ongoing research is completed.

Conflicts of Interest: The authors declare that they have no competing interests.

Abbreviations

The following abbreviations are used in this manuscript:

IARC	International Agency for Research on Cancer
HSI	Hyperspectral imaging

DL	Deep learning
FCNN	Fully connected neural network
CNN	Convolutional neural network
ML	Machine learning
VNIR	Visible and near Infrared
SWIR	Short-wave infrared
SVM	Support vector machines
UV	Ultraviolet
VIS	Visible infrared
NIR	Near infrared
UFC	Colony-forming unit
ROI	Region of interest
CWT	Complex Morlet wavelet
AI	Artificial intelligence
CPU	Central processing unit
GPU	Graphic processing unit
ReLU	rectified linear unit
AUC	Area under the curve
ROC	Receiver operating characteristic
CO ₂	Carbon dioxide
KWh	KiloWatt per hour
RAM	Random access memory

References

1. Winter, G.; Pereg, L. A review on the relation between soil and mycotoxins: Effect of aflatoxin on field, food and finance. *Eur. J. Soil Sci.* **2019**, *70*, 882–897. [CrossRef]
2. Gourama, H.; Bullerman, L.B. *Aspergillus flavus* and *Aspergillus parasiticus*: Aflatoxigenic Fungi of Concern in Foods and Feeds: A Review. *J. Food Prot.* **1995**, *58*, 1395–1404. [CrossRef] [PubMed]
3. Magnussen, A.; Parsi, M.A. Aflatoxins, hepatocellular carcinoma and public health. *World J. Gastroenterol.* **2013**, *19*, 1508. [CrossRef]
4. International Agency for Research on Cancer (IARC). Agents Classified by the IARC Monographs. 2014. Available online: <https://publications.iarc.fr/123> (accessed on 26 May 2024).
5. Kowalska, A.; Walkiewicz, K.; Koziel, P.; Muc-Wierzgoń, M. Aflatoxins: Characteristics and impact on human health. *Adv. Hyg. Exp. Med.* **2017**, *71*, 315–327. [CrossRef]
6. Arastehfar, A.; Carvalho, A.; Houbraken, J.; Lombardi, L.; Garcia-Rubio, R.; Jenks, J.; Rivero-Menendez, O.; Aljohani, R.; Jacobsen, I.; Berman, J.; et al. *Aspergillus fumigatus* and aspergillosis: From basics to clinics. *Stud. Mycol.* **2021**, *100*, 100115. [CrossRef]
7. Garcia-Giraldo, A.M.; Mora, B.L.; Loaiza-Castaño, J.M.; Cedano, J.A.; Rosso, F. Invasive fungal infection by *Aspergillus flavus* in immunocompetent hosts: A case series and literature review. *Med. Mycol. Case Rep.* **2019**, *23*, 12–15. [CrossRef]
8. Diener, U.L.; Cole, R.J.; Sanders, T.H.; Payne, G.A.; Lee, L.S.; Klich, M.A. Epidemiology of aflatoxin formation by *Aspergillus flavus*. *Annu. Rev. Phytopathol.* **1987**, *25*, 249–270. [CrossRef]
9. Ministerio de Agricultura. Encuesta sobre Superficies y Rendimientos de Cultivos. 2023. Available online: <https://www.mapa.gob.es/es/estadistica/temas/estadisticas-agrarias/agricultura/esyrce/default.aspx> (accessed on 6 August 2024).
10. FAO. FAO Statistics. 2023. Available online: <https://www.fao.org/faostat/es/#data/QCL> (accessed on 1 August 2024).
11. Jafari, M.; López-Corrales, M.; Galán, A.J.; Galván, A.I.; Hosomi, A.; Ikegami, H.; Balas, F.; Serradilla, M.J.; Garza-Alonso, C.A.; Yavari, A.; et al. *Orchard Establishment and Management*; CABI: Wallingford, UK, 2022; pp. 184–230. [CrossRef]
12. Galván, A.; Serradilla, M.; Córdoba, M.; Domínguez, G.; Galán, A.; López-Corrales, M. Implementation of super high-density systems and suspended harvesting meshes for dried fig production: Effects on agronomic behaviour and fruit quality. *Sci. Hortic.* **2021**, *281*, 109918. [CrossRef]
13. Abdolahi-pour, M.; Kamgar-Haghighi, A.A.; Sepaskhah, A.R.; Zand-Parsa, S.; Honar, T.; Razzaghi, F. Time and amount of supplemental irrigation at different distances from tree trunks influence on morphological characteristics and physiological responses of rainfed fig trees under drought conditions. *Sci. Hortic.* **2019**, *253*, 241–254. [CrossRef]
14. García, L.; Parra, L.; Jimenez, J.M.; Lloret, J.; Lorenz, P. IoT-Based Smart Irrigation Systems: An Overview on the Recent Trends on Sensors and IoT Systems for Irrigation in Precision Agriculture. *Sensors* **2020**, *20*, 1042. [CrossRef]
15. Abdolahi-pour, M.; Kamgar-Haghighi, A.; Sepaskhah, A.; Dalir, N.; Shabani, A.; Honar, T.; Jafari, M. Supplemental irrigation and pruning influence on growth characteristics and yield of rainfed fig trees under drought conditions. *Fruits* **2019**, *74*, 282–293. [CrossRef]
16. Khozaie, M.; Sepaskhah, A. Economic analysis of the optimal level of supplemental irrigation for rain-fed figs. *Iran Agric. Res.* **2018**, *37*, 17–26.

17. Galván, A.I.; Rodríguez, A.; Martín, A.; Serradilla, M.; Martínez-Dorado, A.; Córdoba, M. Effect of Temperature During Drying and Storage of Dried Figs on Growth, Gene Expression and Aflatoxin Production. *Toxins* **2021**, *13*, 134. [\[CrossRef\]](#)
18. Galván, A.I.; Hernández, A.; de Guía Córdoba, M.; Martín, A.; Serradilla, M.J.; López-Corrales, M.; Rodríguez, A. Control of toxigenic *Aspergillus* spp. in dried figs by volatile organic compounds (VOCs) from antagonistic yeasts. *Int. J. Food Microbiol.* **2022**, *376*, 109772. [\[CrossRef\]](#)
19. Tejero, P.; Martín, A.; Rodríguez, A.; Galván, A.I.; Ruiz-Moyano, S.; Hernández, A. In Vitro Biological Control of *Aspergillus flavus* by *Hanseniaspora opuntiae* L479 and *Hanseniaspora uvarum* L793, Producers of Antifungal Volatile Organic Compounds. *Toxins* **2021**, *13*. [\[CrossRef\]](#)
20. Özer, K.B. 19 Mycotoxins in Fig. In *Advances in Fig Research and Sustainable Production*; CABI: Wallingford, UK, 2022; p. 318.
21. Landgrebe, D. Information extraction principles and methods for multispectral and hyperspectral image data. In *Information Processing for Remote Sensing*; World Scientific: Singapore, 1999; pp. 3–37.
22. ElMasry, G.; Sun, D.W. Principles of hyperspectral imaging technology. In *Hyperspectral Imaging for Food Quality Analysis and Control*; Elsevier: Amsterdam, The Netherlands, 2010; pp. 3–43.
23. LeCun, Y.; Bengio, Y.; Hinton, G. Deep learning. *Nature* **2015**, *521*, 436–444. [\[CrossRef\]](#)
24. Goodfellow, I.; Bengio, Y.; Courville, A. *Deep Learning*; MIT Press: Cambridge, MA, USA, 2016.
25. Chen, Y.; Lin, Z.; Zhao, X.; Wang, G.; Gu, Y. Deep learning-based classification of hyperspectral data. *IEEE J. Sel. Top. Appl. Earth Obs. Remote Sens.* **2014**, *7*, 2094–2107. [\[CrossRef\]](#)
26. Signoroni, A.; Savardi, M.; Baronio, A.; Benini, S. Deep learning meets hyperspectral image analysis: A multidisciplinary review. *J. Imaging* **2019**, *5*, 52. [\[CrossRef\]](#)
27. Khan, A.; Vibhute, A.D.; Mali, S.; Patil, C.H. A systematic review on hyperspectral imaging technology with a machine and deep learning methodology for agricultural applications. *Ecol. Inform.* **2022**, *69*, 101678. [\[CrossRef\]](#)
28. Barbedo, J.G.A. A review on the combination of deep learning techniques with proximal hyperspectral images in agriculture. *Comput. Electron. Agric.* **2023**, *210*, 107920. [\[CrossRef\]](#)
29. Zhong, Z.; Li, J.; Luo, Z.; Chapman, M. Spectral-spatial residual network for hyperspectral image classification: A 3-D deep learning framework. *IEEE Trans. Geosci. Remote Sens.* **2017**, *56*, 847–858. [\[CrossRef\]](#)
30. Paoletti, M.; Haut, J.; Plaza, J.; Plaza, A. Deep learning classifiers for hyperspectral imaging: A review. *ISPRS J. Photogramm. Remote Sens.* **2019**, *158*, 279–317. [\[CrossRef\]](#)
31. Radoglou-Grammatikis, P.; Sarigiannidis, P.; Lagkas, T.; Moscholios, I. A compilation of UAV applications for precision agriculture. *Comput. Netw.* **2020**, *172*, 107148. [\[CrossRef\]](#)
32. Cisternas, I.; Velásquez, I.; Caro, A.; Rodríguez, A. Systematic literature review of implementations of precision agriculture. *Comput. Electron. Agric.* **2020**, *176*, 105626. [\[CrossRef\]](#)
33. Liu, W.; Shao, X.F.; Wu, C.H.; Qiao, P. A systematic literature review on applications of information and communication technologies and blockchain technologies for precision agriculture development. *J. Clean. Prod.* **2021**, *298*, 126763. [\[CrossRef\]](#)
34. Rivera, G.; Porras, R.; Florencia, R.; Sánchez-Solis, J.P. LiDAR applications in precision agriculture for cultivating crops: A review of recent advances. *Comput. Electron. Agric.* **2023**, *207*, 107737. [\[CrossRef\]](#)
35. Peyghambari, S.; Zhang, Y. Hyperspectral remote sensing in lithological mapping, mineral exploration, and environmental geology: An updated review. *J. Appl. Remote Sens.* **2021**, *15*, 031501. [\[CrossRef\]](#)
36. Jia, J.; Wang, Y.; Chen, J.; Guo, R.; Shu, R.; Wang, J. Status and application of advanced airborne hyperspectral imaging technology: A review. *Infrared Phys. Technol.* **2020**, *104*, 103115. [\[CrossRef\]](#)
37. ul Rehman, A.; Qureshi, S.A. A review of the medical hyperspectral imaging systems and unmixing algorithms' in biological tissues. *Photodiagnosis Photodyn. Ther.* **2021**, *33*, 102165. [\[CrossRef\]](#)
38. Lu, Y.; Saeys, W.; Kim, M.; Peng, Y.; Lu, R. Hyperspectral imaging technology for quality and safety evaluation of horticultural products: A review and celebration of the past 20-year progress. *Postharvest Biol. Technol.* **2020**, *170*, 111318. [\[CrossRef\]](#)
39. Wang, B.; Sun, J.; Xia, L.; Liu, J.; Wang, Z.; Li, P.; Guo, Y.; Sun, X. The applications of hyperspectral imaging technology for agricultural products quality analysis: A review. *Food Rev. Int.* **2023**, *39*, 1043–1062. [\[CrossRef\]](#)
40. Sahoo, R.N.; Ray, S.S.; Manjunath, K.R. Hyperspectral remote sensing of agriculture. *Curr. Sci.* **2015**, *108*, 848–859.
41. Jia, B.; Wang, W.; Ni, X.; Lawrence, K.C.; Zhuang, H.; Yoon, S.C.; Gao, Z. Essential processing methods of hyperspectral images of agricultural and food products. *Chemom. Intell. Lab. Syst.* **2020**, *198*, 103936. [\[CrossRef\]](#)
42. Feng, Y.Z.; Sun, D.W. Application of hyperspectral imaging in food safety inspection and control: A review. *Crit. Rev. Food Sci. Nutr.* **2012**, *52*, 1039–1058. [\[CrossRef\]](#)
43. Ferentinos, K.P. Deep learning models for plant disease detection and diagnosis. *Comput. Electron. Agric.* **2018**, *145*, 311–318. [\[CrossRef\]](#)
44. Wang, C.; Liu, B.; Liu, L.; Zhu, Y.; Hou, J.; Liu, P.; Li, X. A review of deep learning used in the hyperspectral image analysis for agriculture. *Artif. Intell. Rev.* **2021**, *54*, 5205–5253. [\[CrossRef\]](#)
45. Wieme, J.; Mollazade, K.; Malounas, I.; Zude-Sasse, M.; Zhao, M.; Gowen, A.; Argyropoulos, D.; Fountas, S.; Van Beek, J. Application of hyperspectral imaging systems and artificial intelligence for quality assessment of fruit, vegetables and mushrooms: A review. *Biosyst. Eng.* **2022**, *222*, 156–176. [\[CrossRef\]](#)
46. Zhou, L.; Zhang, C.; Liu, F.; Qiu, Z.; He, Y. Application of deep learning in food: A review. *Compr. Rev. Food Sci. Food Saf.* **2019**, *18*, 1793–1811. [\[CrossRef\]](#)

47. Wang, X.; Bouzembrak, Y.; Lansink, A.O.; van der Fels-Klerx, H. Application of machine learning to the monitoring and prediction of food safety: A review. *Compr. Rev. Food Sci. Food Saf.* **2022**, *21*, 416–434. [CrossRef]
48. Kumar, A.; Pathak, H.; Bhadauria, S.; Sudan, J. Aflatoxin contamination in food crops: Causes, detection, and management: A review. *Food Prod. Process. Nutr.* **2021**, *3*, 1–9. [CrossRef]
49. Siedliska, A.; Baranowski, P.; Zubik, M.; Mazurek, W.; Sosnowska, B. Detection of fungal infections in strawberry fruit by VNIR/SWIR hyperspectral imaging. *Postharvest Biol. Technol.* **2018**, *139*, 115–126. [CrossRef]
50. Femenias, A.; Gatiús, F.; Ramos, A.J.; Teixido-Orries, I.; Marín, S. Hyperspectral imaging for the classification of individual cereal kernels according to fungal and mycotoxins contamination: A review. *Food Res. Int.* **2022**, *155*, 111102. [CrossRef] [PubMed]
51. Han, Z.; Gao, J. Pixel-level aflatoxin detecting based on deep learning and hyperspectral imaging. *Comput. Electron. Agric.* **2019**, *164*, 104888. [CrossRef]
52. Gao, J.; Zhao, L.; Li, J.; Deng, L.; Ni, J.; Han, Z. Aflatoxin rapid detection based on hyperspectral with 1D-convolution neural network in the pixel level. *Food Chem.* **2021**, *360*, 129968. [CrossRef]
53. Ma, J.; Guan, Y.; Xing, F.; Eltzov, E.; Wang, Y.; Li, X.; Tai, B. Accurate and non-destructive monitoring of mold contamination in foodstuffs based on whole-cell biosensor array coupling with machine-learning prediction models. *J. Hazard. Mater.* **2023**, *449*, 131030. [CrossRef]
54. Kim, Y.K.; Baek, I.; Lee, K.M.; Kim, G.; Kim, S.; Kim, S.Y.; Chan, D.; Herrman, T.J.; Kim, N.; Kim, M.S. Rapid Detection of Single-and Co-Contaminant Aflatoxins and Fumonisin in Ground Maize Using Hyperspectral Imaging Techniques. *Toxins* **2023**, *15*, 472. [CrossRef]
55. Kılıç, C.; İnnér, B. A novel method for non-invasive detection of aflatoxin contaminated dried figs with deep transfer learning approach. *Ecol. Inform.* **2022**, *70*, 101728. [CrossRef]
56. Kılıç, C.; Özer, H.; İnnér, B. Real-time detection of aflatoxin-contaminated dried figs using lights of different wavelengths by feature extraction with deep learning. *Food Control* **2024**, *156*, 110150. [CrossRef]
57. Antoine, J.P.; Carrette, P.; Murenzi, R.; Piette, B. Image analysis with two-dimensional continuous wavelet transform. *Signal Process.* **1993**, *31*, 241–272. [CrossRef]
58. Code Carbon. Codecarbon: Track and Reduce Your Carbon Emissions. 2019. Available online: <https://codecarbon.io> (accessed on 7 August 2024).
59. Bouza, L.; Bugeau, A.; Lannelongue, L. How to estimate carbon footprint when training deep learning models? A guide and review. *Environ. Res. Commun.* **2023**, *5*, 115014. [CrossRef]

Disclaimer/Publisher’s Note: The statements, opinions and data contained in all publications are solely those of the individual author(s) and contributor(s) and not of MDPI and/or the editor(s). MDPI and/or the editor(s) disclaim responsibility for any injury to people or property resulting from any ideas, methods, instructions or products referred to in the content.